Citation for published version:
Gao, J, Ma, XZ, Dong, G, Zang, J, Zhou, X & Zhou, L 2019, 'Topographic influences on transient harbor oscillations excited by N-waves', *Ocean Engineering*, vol. 192, 106548.
https://doi.org/10.1016/j.oceaneng.2019.106548

DOI:
10.1016/j.oceaneng.2019.106548

Publication date:
2019

Document Version
Peer reviewed version

Link to publication

Publisher Rights
CC BY-NC-ND

University of Bath

Alternative formats
If you require this document in an alternative format, please contact:
openaccess@bath.ac.uk

General rights
Copyright and moral rights for the publications made accessible in the public portal are retained by the authors and/or other copyright owners and it is a condition of accessing publications that users recognise and abide by the legal requirements associated with these rights.

Take down policy
If you believe that this document breaches copyright please contact us providing details, and we will remove access to the work immediately and investigate your claim.

Download date: 05. May. 2023

Topographic influences on transient harbor oscillations excited by N-waves

Junliang Gao [1, 2, 3], Xiaozhou Ma [2 *], Guohai Dong [2], Jun Zang [3], Xiaojun Zhou [1], Li Zhou [1]

1. School of Naval Architecture and Ocean Engineering, Jiangsu University of Science and Technology, Zhenjiang 212003, China.

2. State Key Laboratory of Coastal and Offshore Engineering, Dalian University of Technology, Dalian 116024, China.

3. Research Unit for Water, Environment and Infrastructure Resilience (WEIR), Department of Architecture and Civil Engineering, University of Bath, BA2 7AY, U.K.

Abstract:

The main objective of this paper is to comprehensively study influences of the variation of the bottom profile inside the harbor on the transient harbor oscillations excited by normally-incident N-waves. The specific physical phenomena investigated consist of wave profile evolution, maximum runup, relative wave energy distribution and total wave energy inside the harbor. A series of numerical experiments are implemented using a fully nonlinear Boussinesq model, FUNWAVE-TVD. Results show that when the harbor is subjected to the leading-elevation N-waves (LEN waves), the evolution of the maximum free surface elevation during the wave shoaling process inside the harbor coincides well with Green's law overall. When the incident wave amplitude is small, the maximum runup inside the harbor is almost only determined by the incident wave amplitude. As the incident wave amplitude increases, effects of the bottom profile on the maximum runup closely depend on both the incident wave type and amplitude. As the mean water depth inside the harbor decreases, the relative wave energy distribution tends to become more uniform, regardless of the incident wave amplitude and type. Finally, the variation trend of the total wave energy with the bottom profile is found to depend on the incident wave amplitude.

Key Words:

Harbor oscillations; Harbor resonance; N-waves; topographic variation; Numerical simulation; FUNWAVE-TVD

*Corresponding author. Tel.: +86 411 8470 7262; fax: +86 411 847 08526. E-mail address: maxzh@dlut.edu.cn.

1. Introduction

Harbor oscillations (also termed as *harbor resonance*) refer to the phenomenon that wave energy is trapped and amplified inside semi-enclosed water bodies, such as bays or harbors. It may be triggered by infragravity waves, atmospheric fluctuations, short wave groups, shear flow and tsunamis propagating into bays or harbors (Bellotti et al., 2012; De Jong and Battjes, 2004; Dong et al., 2010a, b; Fabrikant, 1995; Gao et al., 2018b; Gao et al., 2019; Liu et al., 2003; Okihiro and Guza, 1996; Wang et al., 2011). Via generating excessive movements of vessels moored inside the harbor, oscillations may interfere with dock operations and create overlarge mooring forces that may break mooring lines (Kumar et al., 2016; López and Iglesias, 2014). Recent progress on the modeling and understanding of this phenomenon has been reviewed in Rabinovich (2009).

Among various inducing factors, the transient harbor resonance induced by tsunamis usually has destructive effects. Tsunamis may be triggered by offshore landslides, submarine earthquakes, undersea volcanic eruptions, or other kinds of disturbances, such as onshore landslides falling into water or meteors falling into the open sea, etc. As tsunamis reach the nearshore zone, due to the continuously decreasing water depth and the durative focus of the wave energy, their wave heights are often remarkably enlarged (Zhao et al., 2012). Take the Indian Ocean tsunami triggered by the Sumatra earthquake on 26 December, 2004, for example. It propagated for about two hours to Colombo harbor of Sri Lanka, exciting extreme oscillations with a resonant period of about 75 min and a maximum wave height of 3.87 m; it also propagated for about fourteen hours to Bunbury harbor of Australia, triggering oscillations with a maximum wave height of 1.75 m (Pattiaratchi and Wijeratne, 2009). Therefore, to reduce the interference with the normal harbor operation and minimize the possible destructive effects, a further research effort is essential to improve current understanding for this kind of harbor oscillations and thus enhance our predictive capability.

Because some features in the tsunami events (such as the stable hump-like waveforms after a long distance of propagation) can be well simulated by solitary waves, lots of experimental, numerical and theoretical investigations on solitary waves have been associated to tsunamis for decades (e.g., Camfield and Street (1969); Goring (1978); Hsiao et al. (2008); Liu et al. (1995); Lo et al. (2013); Seiffert et al. (2014); Synolakis (1987); Yao et al. (2018a); Yao et al. (2018b)). However, several field observations found that the leading tsunami wave was usually preceded by

a depression. According to these field observations and in order to gain better geophysical relevancy, the concept of N-waves was first proposed by Tadepalli and Synolakis (1994). Subsequently, owing to increasing evidences from field observations, it has been generally believed that the leading tsunami wave approaches nearshore zones like either leading-depression N-waves (LDN waves) or leading-elevation N-waves (LEN waves). Recently, based on the viewpoint that the time and the length scales of real tsunamis are considerably dissimilar or inconsistent with those of solitary waves, whether main features of real tsunamis in tsunami events could be fully represented by the classical solitary wave theory was also doubted by Madsen and Schäffer (2010). Tadepalli and Synolakis (1994) and Madsen and Schäffer (2010) proposed different expressions to describe N-wave profiles.

Hitherto, studies on the transient harbor resonance induced by tsunamis are mainly confined to utilizing solitary waves to represent real tsunamis (e. g., Dong et al. (2010a); Gao et al. (2016a); Gao et al. (2018a); Gao et al. (2016b)). In addition, the coastal influences related to N-waves are only limited to estimating their runup and rundown on plane beaches (e. g., Charvet et al. (2013); Madsen and Schäffer (2010); Tadepalli and Synolakis (1994); Zhao et al. (2012)). As far as the authors know, investigations of the transient harbor oscillations triggered by N-waves are extremely rare so far. Gao et al. (2017) introduced N-waves for the first time to the studies of the transient harbor resonance excited by tsunamis, and the influences of both the amplitude and the type of the incident N-waves on the relative wave energy distribution and the maximum runup/rundown of the incident waves inside the harbor were discussed. Except Gao et al. (2017), the authors have not yet seen more studies on the harbor resonance excited by N-waves.

To further enhance the understanding about tsunami-induced oscillations, this paper adopts N-waves to explore related transient resonance phenomena as well. The focus of this article is to comprehensively investigate influences of the bottom profile inside the harbor on the wave profile evolution, the maximum runup, the relative wave energy distribution and the total wave energy during the transient harbor resonance excited by normally-incident N-waves with various amplitudes. It should be stressed that it is critical to accurately predict and systematically investigate the wave profile evolution, the maximum runup, the relative wave energy distribution and the total wave energy inside the harbor during the transient oscillations excited by tsunamis. The wave profile evolution and the maximum runup inside the harbor are closely related to the

tsunami-induced inundation near the port zone (Gao et al., 2017; Gao et al., 2016a), and important hydrodynamic information can be provided by the relative wave energy distribution and the total wave energy for estimating the movements of the moored ships inside the harbor (Kumar et al., 2016; López and Iglesias, 2014).

Compared to Gao et al. (2017) that has investigated the transient harbor resonance induced by N-waves, there are mainly three research developments in this article. First, in Gao et al. (2017), only flat bottom inside the harbor was adopted. In fact, the bottom inside real harbors is usually uneven on most occasions (Kumar and Gulshan, 2018; Wang et al., 2013; Wang et al., 2014). Hence, in the present study, complex bathymetries inside the harbor are further considered. Second, in Gao et al. (2017), the amplitudes of the incident N-waves were relatively small and the wave fields inside the harbor were only limited to weakly nonlinear wave conditions; while in this article, the wave condition inside the harbor is extended to strong wave nonlinearity. Third, studies on the wave profile evolution and the total wave energy inside the harbor excited by the incident N-waves are taken into consideration for the first time in the present work. All numerical experiments in this paper are carried out by utilizing the fully nonlinear Boussinesq model proposed by Shi et al. (2012). For simplification, the harbor is assumed to be long and narrow; the free surface movement inside the harbor then essentially becomes one-dimensional.

The rest of the paper is organized as follows. In Section 2, the numerical model and the data analysis technique are described. The former will be validated by an analytical solution and physical experimental data. In Section 3, the incident wave parameters and the setup of the numerical wave tank are presented. In Section 4, the simulation results are analyzed and explained in detail. Main conclusions based on these results are given in Section 5.

2. Numerical model and data analysis technique

2.1. Numerical model

2.1.1. Model description

All numerical simulations in this article are implemented by utilizing the well-known and widely-used FUNWAVE-TVD model. The model was proposed and developed at Center for Applied Coastal Research of University of Delaware by Shi et al. (2012). The fully nonlinear Boussinesq equations of Chen (2006) are chosen as the governing equations which further

incorporate a moving reference level as in Kennedy et al. (2001) and are solved by adopting a hybrid finite difference - finite volume scheme. The governing equations are re-organized to easily implement a high-order shock-capturing TVD (Total Variation Diminishing)-type scheme, which allows the model to simulate wave breaking without relying on empirical formulas (Ma et al., 2012; Shi et al., 2012). A third-order strong stability-preserving Runge–Kutta scheme is used for adaptive time stepping. The model is parallelized adopting the Message Passing Interface with non-blocking communication.

With the above-mentioned improvements, FUNWAVE-TVD has become more powerful in estimating wave hydrodynamic processes in the offshore and nearshore zones, including wave diffraction, shoaling, refraction, breaking as well as wave runup/rundown on the plane and natural beaches (Shi et al., 2012; Su et al., 2015). To examine the ability of the model to simulate the transient harbor resonance triggered by tsunamis, the present numerical model was adopted by Gao et al. (2017) to reproduce the laboratorial and numerical experiments of Dong et al. (2010a). The maximum runups inside the harbor predicted by FUNWAVE-TVD were compared with the numerical and experimental data of Dong et al. (2010a), and fairly good coincidence between them was found, which indicates that the present model can reproduce the transient harbor resonance induced by tsunamis accurately.

2.1.2. Model verification

Although Gao et al. (2017) has examined the capacity of the present model to predict the maximum runups of the incident tsunamis inside the harbor. However, the incident tsunami wave heights considered in Gao et al. (2017) were relatively small and the wave climates inside the harbor were restricted to weakly nonlinear wave conditions. While in this paper, the wave condition inside the harbor is extended to strong wave nonlinearity. Hence, it is essential to further verify the capability of the present model to estimate the maximum runups of tsunami waves on a vertical wall under condition of strong wave nonlinearity.

The runup of solitary waves on a fully reflective vertical wall is a classical wave-structure interaction problem. The maximum runup of solitary waves with various amplitudes on the vertical wall, A_u, was studied experimentally by Camfield and Street (1969). Subsequently, based on the nonlinear superposition of oppositely travelling solitary waves, a second-order theoretical

solution of the maximum runup, expressed as $\frac{A_u}{h}=2\frac{A_0}{h}+\frac{1}{2}\left(\frac{A_0}{h}\right)^2$, was deduced by Byatt-Smith (1971). A_0 and h denote the incident wave amplitude and the water depth, respectively. In the current verification, a series of simulations are carried out for solitary waves with various amplitudes. The water depth, h, is set to a constant, 1.0 m. In order to assure that the incident solitary waves of all amplitudes travel freely over a long enough distance before impacting on the vertical wall, the computational domain is set to have a length of 100 m. The origin of the Cartesian coordinate system (o, x, z) is placed at the still water level with z measured upward, and x=0 is defined at the left boundary of the domain with its positive direction pointing to the right boundary (i.e., at x=100 m) where the vertical wall hit by the incident solitary wave is deployed.

The theoretical expression of the incident solitary wave can be formulated as follows (Madsen et al., 2008):

$$\eta(x,t)=A_0\mathrm{sech}^2\left[k\left(x-x_0-ct\right)\right], \tag{1}$$

where $k=\sqrt{\frac{3A_0}{4h^3}}$ and $c=\sqrt{g\left(h+A_0\right)}$. x_0 is the center position of the initial incident solitary wave, and g is the acceleration due to the gravity. Therefore, the initial incident solitary wave used in the numerical model is expressed as

$$\eta(x,t=0)=A_0\mathrm{sech}^2\left[k\left(x-x_0\right)\right], \tag{2}$$

and the initial water particle velocity takes a linear relationship with the initial incident free surface elevation, i.e.,

$$u(x,t=0)=\sqrt{\frac{g}{h}}\eta(x,t=0). \tag{3}$$

The center position of the initial incident solitary wave is always placed at the middle of the computational domain (i.e., x_0=50 m). Two wave gauges are deployed inside the domain. One is arranged at x=75 m for measuring the incident wave and the other is placed at the vertical wall for recording the maximum runup. A uniform grid size of Δx=0.05 m is adopted for all the simulations. Each case is terminated after the incident wave hits and reflects from the wall at x=100 m.

Fig. 1 compares the time series of the simulated and theoretical incident solitary waves with A_0=0.025 m. It is clear that the solitary wave produced in the numerical model coincides fairly well with the theoretical formula. Fig. 2 further compares the simulated maximum runups with the second-order theoretical solution of Byatt-Smith (1971) and the experimental data of Camfield and

Street (1969). It is obvious that, overall, the present predicting results show good coincidence with both the theoretical solution and the experimental data at the range of the wave nonlinearity considered here (i.e., $A_u/h<0.75$).

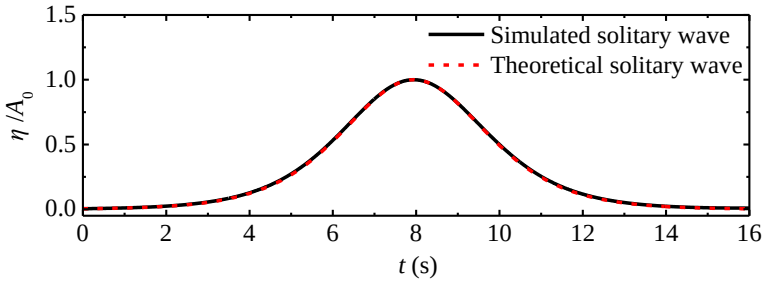

Fig. 1. Comparison of the time series of the simulated and the theoretical incident solitary waves with A_0=0.025 m

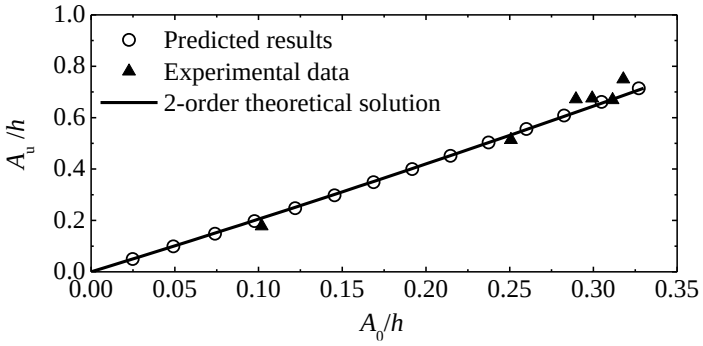

Fig. 2. The maximum runups of solitary waves on the vertical wall

2.2. Data analysis technique

As mentioned in Section 1, the wave profile evolution, the maximum runup of the incident N-waves, the relative wave energy distribution and the total wave energy inside the harbor are considered in the present study. Both the wave profile evolution and the maximum runup of the incident N-waves can be investigated via directly reading the maximum/minimum free surface elevations which are measured by a set of wave gauges deployed inside the harbor. However, to analyze the wave energy distribution and the total wave energy inside the harbor during the transient harbor oscillations triggered by N-waves, a specialized data analysis technique (i.e., the normal mode decomposition method), is necessary to be adopted.

In order to predict the natural frequencies, the modal shapes and the response amplitudes of

various resonant modes inside natural bays or harbors which are exposed to tsunamis, the normal mode decomposition (NMD) method was originally proposed by Sobey (2006). Afterwards, the original NMD method was improved by Gao et al. (2015) to more accurately estimate the natural frequencies and the modal shapes. The method includes two computational steps. The first step estimates the discrete set of natural frequencies f_{n} and the associated modal shapes $\mathbf{X}_{\mathrm{n}}$ of bays or harbors based on a spatially varied Sturm-Liouville equation which is expressed as

$$\frac{1}{b}\frac{d}{dx}\left(S\frac{dX}{dx}\right)+\frac{\omega^2}{g}X=0 \tag{4}$$

for an elongated one-dimensional harbor. The second step involves the computation of the response amplitudes at various resonant modes, which are expressed and solved as a multi-dimensional optimization problem. For the elongated harbor, the response amplitudes are calculated using the following fitting equation

$$\eta(x,t)=\sum_{n}\left[a_{1n}\cos\omega_n t+a_{2n}\sin\omega_n t\right]\mathbf{X}_n(x), \tag{5}$$

where $\omega_{\mathrm{n}}=2\pi f_{\mathrm{n}}$ is the resonant angular frequency. The response amplitudes a_{1n}, a_{2n} would then be available as an optimization problem. The suitable objective function to be minimized would be

$$S(a_{1n},a_{2n})=\sum_{ik}\left[\eta_{ik}-\sum_{n=1}^{M}\left(a_{1n}\cos\omega_n t_k+a_{2n}\sin\omega_n t_k\right)\mathbf{X}_n(x_i)\right]^2, \tag{6}$$

where M denotes the number of modes of which the response amplitudes should be decomposed. The eigenmode amplitudes of different resonant modes are defined as

$$A_n=\left[a_{1n}^2+a_{2n}^2\right]^{1/2}. \tag{7}$$

In this step, the resonant angular frequency ω_{n} and the modal shapes $\mathbf{X}_{\mathrm{n}}$ predicted in the first step are utilized as known variables.

Recently, based on the improved NMD method, Gao et al. (2017; 2016a; 2018a) comprehensively investigated the wave energy distribution over different resonant modes during the transient harbor resonance triggered by various types of tsunamis including solitary waves, successive solitary waves and N-waves. For the detailed theory of this data analysis technique, the interested reader is referred to Gao et al. (2015) and Sobey (2006).

3. Numerical setups

3.1. Incident wave parameters

In this article, the N-wave profiles proposed by Madsen and Schäffer (2010) are adopted as the incident tsunamis propagating from the open sea. In their paper, through superposing two single waves, the N-wave profiles were established. According to whether the trough and the crest of the N-wave have equal amplitude, it can be classified as the generalized and the isosceles N-waves, and both classifications include leading-depression N-waves (LDN waves) and leading-elevation N-waves (LEN waves). In current study, only the isosceles LDN and LEN waves are taken into consideration. In Madsen and Schäffer (2010), the superposition of the positive and the negative solitary waves was considered, and hence the isosceles N-wave took the form as follows:

$$\eta(x, t=0) = \pm A_1 \left\{ \operatorname{sech}^2\left(k_1 \left(x - x_0 \right) - \frac{\pi}{4} \right) - \operatorname{sech}^2\left(k_1 \left(x - x_0 \right) + \frac{\pi}{4} \right) \right\}, k_1 = \sqrt{\frac{3A_1}{4h^3}} . \tag{8}$$

The plus and minus signs in this expression respectively correspond to the LEN and LDN waves. It is emphasized here that A_1 is not the amplitude of the N-wave formulated in Eq. (8). Identical to Eq. (2), if the symbol A_0 is utilized to represent the amplitude of the N-wave, Madsen and Schäffer (2010) also pointed out the following quantitative relationship:

$$A_1 = 1.165 A_0 . \tag{9}$$

Table 1. Wave parameters of the initial incident N-waves and the geometric parameters of the harbors adopted in all the numerical experiments

Group	Initial waveform	A_0 (m)	Topography	Geometrical parameters
A	LEN	0.01, 0.05, 0.10, 0.15, 0.20, 0.25, 0.30	arc-tangent-type	h_1=12 m, h_0=3 m, α=6.4 m, $\bar{h}$ =10.08 m
B				h_1=12 m, h_0=3 m, α=8.0 m, $\bar{h}$ =8.78 m
C			constant slope	h_1=12 m, h_0=3 m, $\bar{h}$ =7.50 m
D			hyperbolic-cosine-type	h_1=12 m, h_0=3 m, κ=0.1, $\bar{h}$ =6.33 m
E				h_1=12 m, h_0=3 m, κ=30.0, $\bar{h}$ =5.23 m
F	LDN	0.01, 0.05, 0.10, 0.15, 0.20, 0.25, 0.30	arc-tangent-type	h_1=12 m, h_0=3 m, α=6.4 m, $\bar{h}$ =10.08 m
G				h_1=12 m, h_0=3 m, α=8.0 m, $\bar{h}$ =8.78 m
H			constant slope	h_1=12 m, h_0=3 m, $\bar{h}$ =7.50 m
I			hyperbolic-cosine-type	h_1=12 m, h_0=3 m, κ=0.1, $\bar{h}$ =6.33 m
J				h_1=12 m, h_0=3 m, κ=30.0, $\bar{h}$ =5.23 m

For all numerical experiments, a constant water depth outside the harbor of h_1=12.0 m is utilized. Under this circumstance, the wave parameters for all the simulations are presented in Table 1. This article consists of ten groups of numerical simulations, i.e., Groups A-J. Each group includes seven cases with various initial wave amplitudes ranging between 0.01 m and 0.30 m to comprehensively study the influence of the wave amplitude on transient harbor oscillations. In Groups A-E, the isosceles LEN waves are utilized as the initial incident waves; while in Groups F-J, the isosceles LDN waves are adopted. The aim of considering Groups F-J in this paper is to reveal the similarities and differences between the transient harbor resonance phenomena induced by LDN waves and LEN waves.

Fig. 3 presents the comparison of the waveforms for these two types of initial incident N-waves with A_0=0.01 m and 0.30 m. The circle in this figure represents the wavefront of the corresponding waveform, which is defined as the position where the free surface elevation is equal to ± 0.05 times the incident wave amplitude A_0. In this article, the wavelength of the N-wave, L_0, is defined as twice the distance between x_0 and the wavefront. As anticipated, for the LDN and LEN waves with the same amplitude, their waveforms are identical except for antiphase. It is also clearly seen that the wavelength of the N-waves with A_0=0.01 m is much larger than that with A_0=0.30 m. The wavelengths for all the incident N-waves with various amplitudes considered in this paper are further presented in Table 2. It is shown that as the wave amplitude A_0 increases from 0.01 m to 0.3 m, the wavelength of the incident N-wave decreases gradually from 2685.0 m to 490.2 m, which is due to the fact that Eq. (8) retains the constrained relationship between the spatial and temporal scales of the wave identical to the classical solitary wave theory.

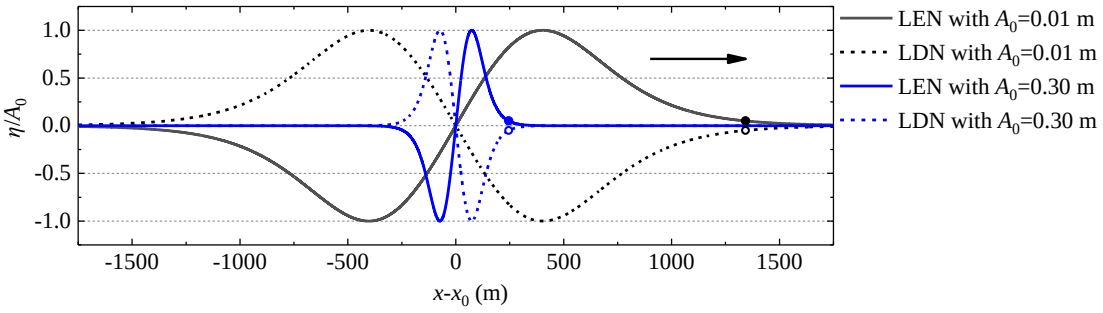

Fig. 3. Waveforms of the initial incident LEN and LDN waves with A_0=0.01 m and 0.30 m. The circle refers to the wavefront of the corresponding waveform.

Table 2. Wavelengths of the incident N-waves with various wave amplitudes

A_0 (m)	0.01	0.05	0.10	0.15	0.20	0.25	0.30
Wavelength (m)	2685.0	1200.8	849.0	693.4	600.4	537.0	490.2

3.2. Numerical wave tank

Fig. 4 illustrates the numerical wave tank (NWT) utilized in the numerical simulations. The dimensions of the NWT are 5500 m × 120 m, and all the boundaries are set to be fully reflective. The harbor has a length of L=1500 m and a width of $2b$=30 m. 151 wave gauges (G_{01}–G_{151}) are equidistantly arranged along the center line of the harbor with a spacing 10.0 m. Gauges G_{01} and G_{151} are placed at the entrance and the backwall of the harbor, respectively. To reduce the computational cost, only half of the domain (i.e., $y \geq 0$) is utilized for simulations because of the geometrical symmetry. The grid sizes of Δx and Δy are uniform in 1.0 m over the entire NWT. Total numbers of the rectangular elements and the grid nodes are 330,000 and 335,561, respectively. For all cases, the wavefront of the initial incident wave is set at the harbor entrance (i.e., $x_0 = -L_0/2$) as an initial condition, and the total simulation time is set to 600 s.

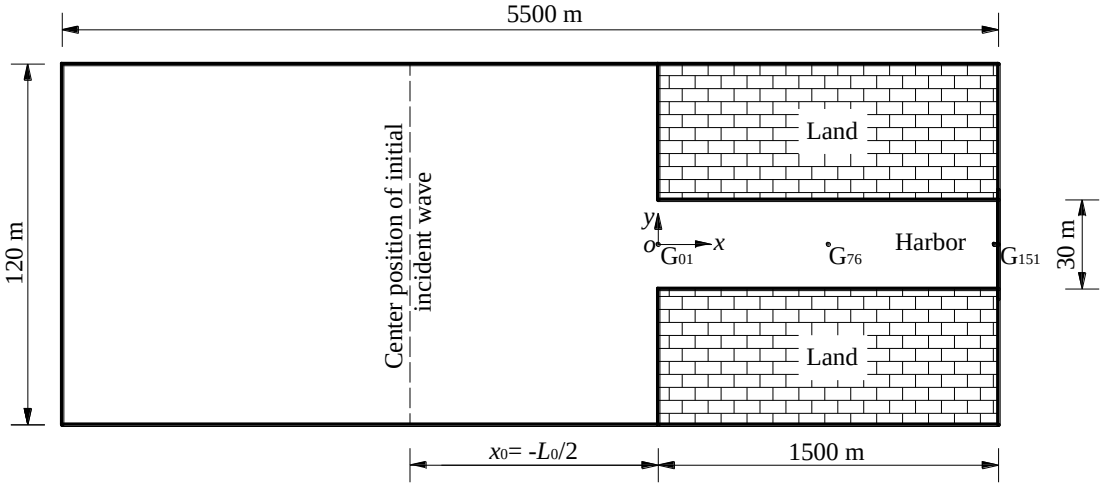

Fig. 4. Schematic plan view of the numerical wave tank (NWT) adopted in numerical simulations. Only half of the NWT (i.e., $y \geq 0$) is utilized as the computational domain for simulations due to its geometrical symmetry with respect to the x-axis.

In order to investigate influences of different topographies inside the harbor on the transient

harbor resonance excited by solitary waves, three types of topographies, i.e., an arc-tangent-type bottom, a plane slope bottom and a hyperbolic-cosine-type bottom, were considered in Gao et al. (2016a). Similarly, these three types of topographies are also utilized in this article to further investigate influences of different topographies inside the harbor on the harbor resonance triggered by N-waves.

The still water depth inside the harbor, $h^{\mathrm{I}}(x)$, is formulated as

$$h^{\mathrm{I}}(x)=\begin{cases} h_0+\alpha\,\mathrm{atan}\left[\beta\left(L-x\right)\right] & \text{arc-tangent-type bottom} \\ h_1-\gamma x & \text{constant slope bottom} \\ h_0\cosh^{\kappa}\left[\mu\left(L-x\right)\right] & \text{hyperbolic-cosine-type bottom} \end{cases}, \tag{10}$$

in which h_0 and h_1 refer to the local water depth at the backwall (i.e., at x=1500 m) and the water depth outside the harbor, respectively, and they are set to 3.0 m and 12.0 m in all simulations. The variables α, β, γ, κ and μ in the above equation are different geometric parameters controlling bottom profiles, and abide by the following constraint relationships:

$$\beta=\frac{1}{L}\tan\left(\frac{h_1-h_0}{\alpha}\right), \tag{11}$$

$$\gamma=\frac{h_1-h_0}{L}, \tag{12}$$

and

$$\mu=\frac{1}{L}\mathrm{acosh}\left[\left(\frac{h_1}{h_0}\right)^{1/\kappa}\right]. \tag{13}$$

Table 1 also lists the type of bottom profile inside the harbor utilized in each group and the corresponding geometric parameter values. $\bar{h}$ in this table refers to the mean water depth inside the harbor, which is calculated as

$$\bar{h}=\frac{1}{b}\int_0^L h^{\mathrm{I}}(x)dx. \tag{14}$$

Fig. 5 presents the comparison of various bottom profiles inside harbors for all groups. The harbor used in Groups A and F has an arc-tangent-type bottom, and the mean water depths inside the harbor is 10.08 m. Similarly, the harbor in Groups B and G also has the arc-tangent-type topography. However, because of a larger value of α, the mean water depth inside the harbor drops to 8.78 m. The harbor in Groups D and I has a hyperbolic-cosine-type bottom, and the mean water depth inside the harbor is 6.33 m. Owing to the increase of κ, although the harbor in Groups E and J also has the hyperbolic-cosine-type topography, the mean water depth decreases to 5.23 m. The

harbor in Groups C and H has a constant slope bottom, and the mean water depth is 7.50 m, which falls in between those of Groups B/G and D/I.

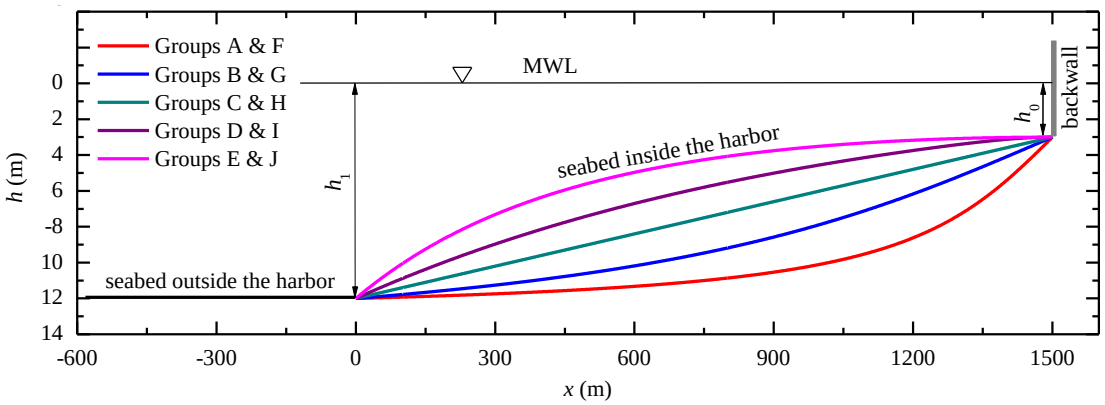

Fig. 5. Various bottom profiles inside the harbor for Groups A-J

4. Results and discussion

4.1. Wave profile evolution inside the harbor

In this section, the wave profile evolution inside the harbor is systematically investigated. Specifically speaking, the variations of the maximum free surface elevations as the incident N-waves propagate from the harbor entrance to the backwall of the harbor are mainly concerned here because they are closely associated with the tsunami-induced inundation near the port zone. It should be noted that for the incident N-waves with A_0=0.01 m and 0.05 m, their wavelengths are extremely long, and equal 1.79 and 0.80 times the length of the harbor, respectively (see Table 2). Under this circumstance, the reflected wave profiles from the backwall will contaminate the incident wave profiles in most area of the harbor, which makes it difficult to distinguish the incident wave profile from the contaminated wave profiles. Hence, all the cases with A_0=0.01 m and 0.05 m are not taken into consideration in this section.

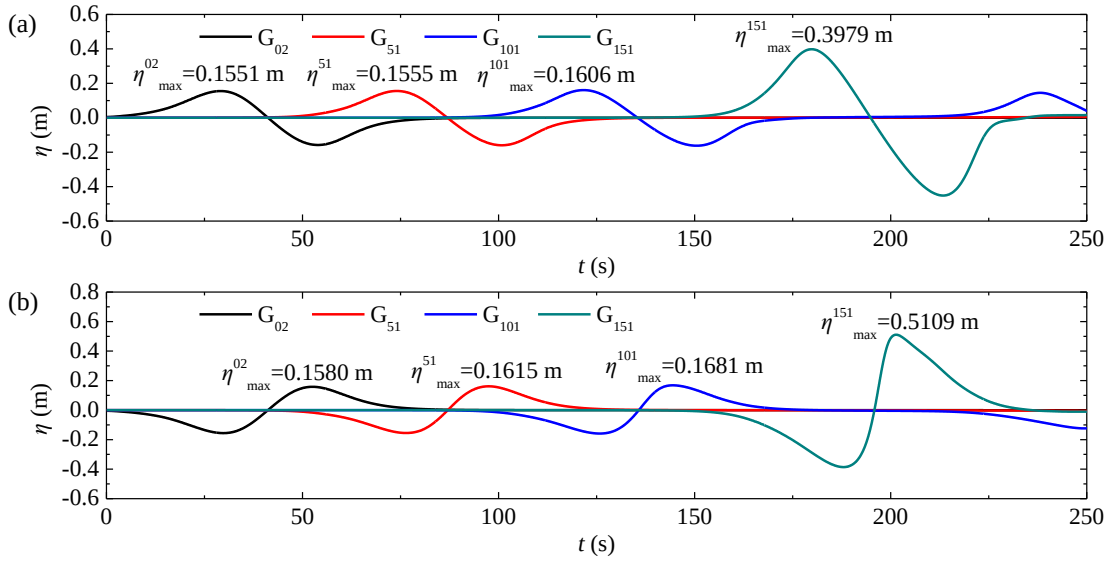

Fig. 6. Time series of the free surface elevations at different wave gauges for the two cases in (a) Group A with A_0=0.1 m and (b) Group F with A_0=0.1 m. η^i_{max} in the figure refers to the maximum free surface elevation at the i^{th} wave gauge.

Fig. 6 presents the time series of the free surface elevations at different wave gauges for the two cases in Groups A and F with A_0=0.1 m. The symbol η^i_{max} in this figure refers to the maximum free surface elevation at the i^{th} wave gauge. These two cases have the identical bottom profile inside the harbor but different types of the incident N-waves (refer to Table 1). For the case shown in Fig. 6a, the harbor is subjected to the incident LEN wave with A_0=0.1 m. The maximum wave elevations at gauges G_{02}, G_{51}, G_{101} and G_{151} are shown to gradually increase as the incident N-wave propagates from the harbor entrance to the backwall because of the continuously decreasing local water depth. For the case shown in Fig. 6b, the harbor is exposed to the incident LDN wave with A_0=0.1 m. Due to the same reason, the maximum wave elevations at gauges G_{02}, G_{51}, G_{101} and G_{151} are also presented to gradually increase. Through comparing Fig. 6a and b, we can also find that the maximum free surface elevations at all the four wave gauges excited by the LDN wave are always larger than the corresponding ones induced by the LEN wave, especially at gauge G_{151} (i.e., at the backwall of the harbor). At gauge G_{151}, the maximum runup over the backwall of the harbor subjected to the LEN wave with A_0=0.1 m is 0.3979 m, while when the harbor is exposed to the LDN wave with the same amplitude, the maximum runup over the backwall increases up to 0.5109 m, being 28.4% larger than the former.

To further present a complete variation tendency of the maximum free surface elevation as the incident N-wave travels from the harbor entrance to the backwall, Fig. 7 demonstrates the evolutions of the maximum free surface elevations inside the harbor for Group A under the conditions of A_0=0.10 m–0.30 m. Among the ten groups of simulations considered in this paper, the harbor used in Group A has the largest mean water depth, i.e. $\bar{h}$=10.08 m. For all these cases in Group A, owing to the gradually decreasing local water depth, as expected, the amplitude of the incident wave gradually increases as it propagates to the backwall. Based on the law of wave energy conservation and the linear long wave theory, if the energy due to the wave reflection is neglected, the amplitude evolution of the linear long wave traveling over a mild slope can be estimated theoretically by

$$\frac{A}{A_R}=\left(\frac{h_R}{h}\right)^{1/4}, \tag{15}$$

where A_R and h_R respectively denote the incident wave amplitude and the local water depth at a certain reference position. This 1/4 power dependence is usually referred to as Green's law (Mei, 1983). The maximum free surface evolution of the incident N-wave estimated by Eq. (15) is also presented in Fig. 7. Considering the boundary influence of the harbor entrance at gauge G_{01}, gauge G_{02} is selected as the reference position during the calculation of Green's law. It is clearly seen that for all the five incident wave amplitudes considered, the estimations of Green's law coincide very well with the simulation results in the whole domain overall, except at the small area where the incident and the reflected waves interact with each other near the backwall.

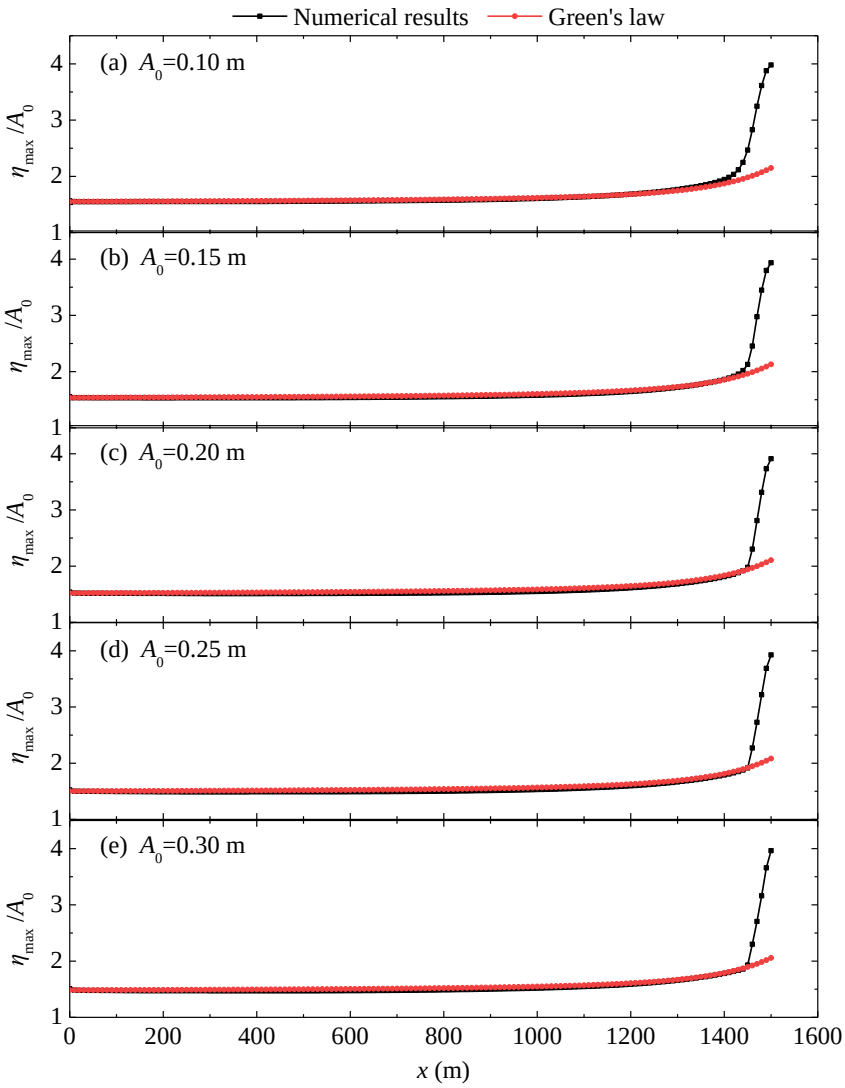

Fig. 7. Evolutions of the maximum free surface elevations inside the harbor for Group A under the conditions of various incident wave amplitudes.

Fig. 8 presents the evolutions of the maximum free surface elevations inside the harbor for Group E under the conditions of A_0=0.10 m–0.30 m. Among the ten groups of simulations considered in this paper, the harbor utilized in Group E has the smallest mean water depth, i.e. $\bar{h}$ =5.23 m. When the incident wave amplitude is small (i.e., A_0=0.1 m), it is also seen that in general, there exists a good coincidence between the prediction of Green's law and the simulation results in the whole domain, except at the small area near the backwall (i.e., 1420 m $< x \leq$ 1500 m). As the incident wave amplitude increases, although Green's law can still predict the evolution of the maximum free surface elevation very well in most of the harbor domain, the area where Green's law obviously underestimates the maximum free surface elevations becomes more and more

expanded. When the incident wave amplitude rises up to A_0=0.30 m, the invalid spatial range of Green's law extends to 800 m <x ≤ 1500 m. Hence, by comparing the phenomena in Figs. 7 and 8, it can be concluded that when the harbor is subjected to the incident LEN waves and the mean water depth inside is relatively large, at the range of the incident wave amplitude considered (i.e., 0.1 m ≤A_0 ≤ 0.3 m), Green's law can predict very well the evolution of the maximum free surface elevation in the whole domain overall, except at the small area near the backwall. On the contrary, when the harbor is suffered from the incident LEN waves but the mean water depth inside is relatively small, the applicability of Green's law becomes closely related to the incident wave amplitude; the larger the incident wave amplitude is, the smaller the valid spatial range of Green's law becomes.

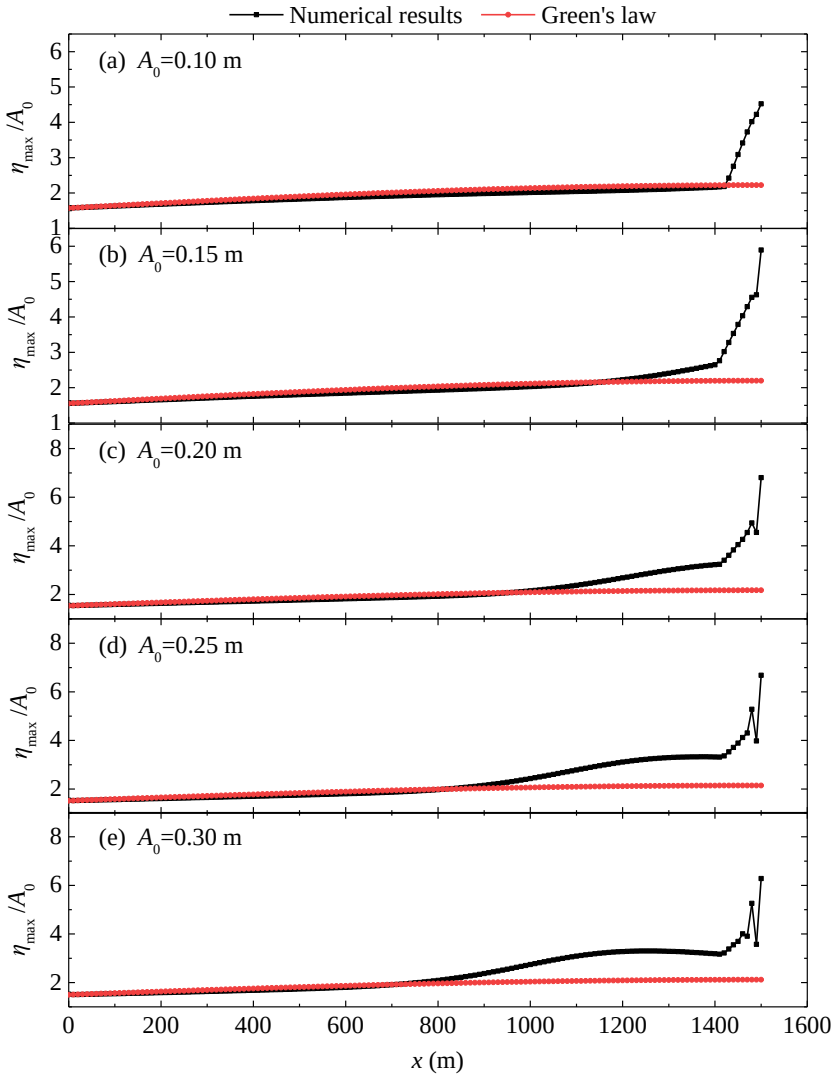

Fig. 8. Evolutions of the maximum free surface elevations inside the harbor for Group E under the conditions of various incident wave amplitudes.

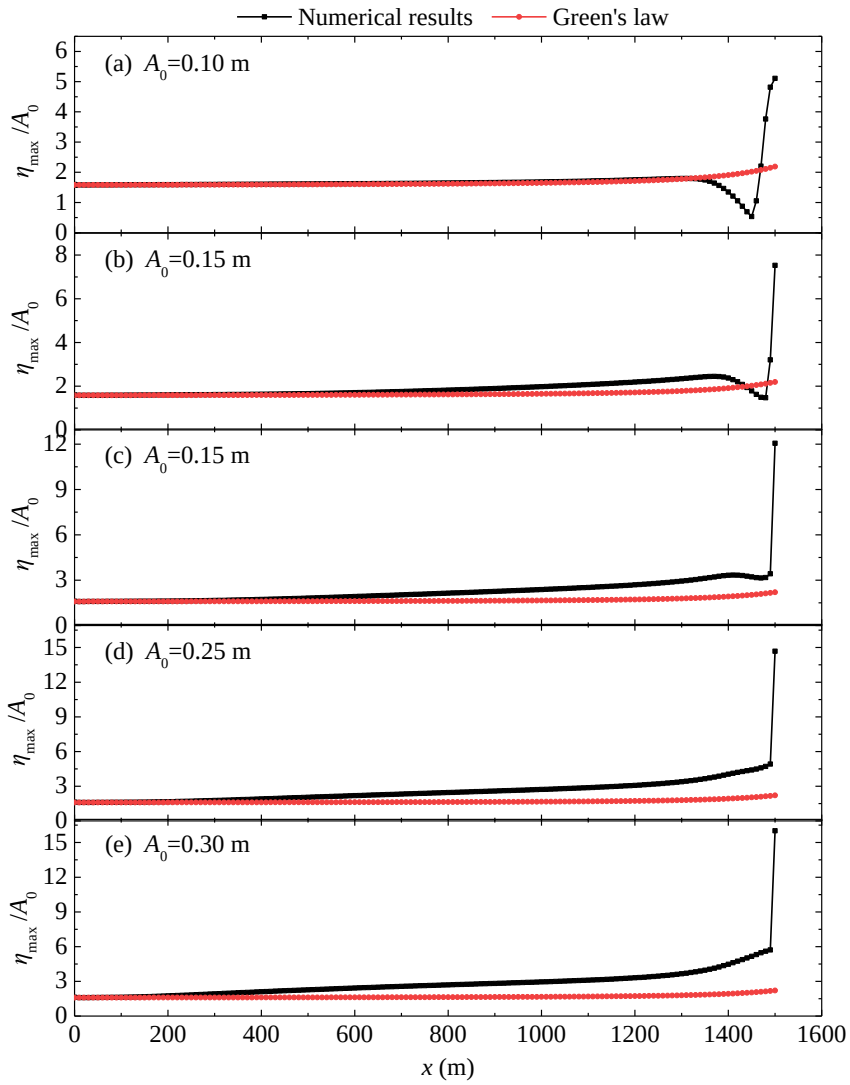

Fig. 9. Evolutions of the maximum free surface elevations inside the harbor for Group F under the conditions of various incident wave amplitudes.

Fig. 9 further shows the evolutions of the maximum free surface elevations inside the harbor for Group F under the conditions of A_0=0.10 m–0.30 m. As mentioned in Section 3, the bottom profile inside the harbor used in Group F is identical to that in Group A, but the incident wave adopted in Group F becomes the LDN wave. It is seen that only when the incident LDN wave has the smallest amplitude (i.e., A_0=0.10 m) (Fig. 9a), Green's law can well predict the evolution of the maximum free surface elevation almost in the entire harbor domain except at the small area where the incident and the reflected waves interact with each other near the backwall. For the larger incident wave amplitude (i.e., $A_0 \geq 0.15$ m) (Fig. 9b-e), Green's law remarkably underestimates the numerical predictions almost in the entire harbor domain except that there is a

small spatial region near the backwall where Green's law overestimates the numerical prediction when A_0=0.15 m. It should be noted that for both A_0=0.10 m and 0.15 m (Fig. 9a and b), there is an obvious decreasing trend of the maximum free surface elevation near the backwall. This is because the reflected leading trough free surface from the backwall interacts with the subsequent incident crest free surface, and the former has similar wave profile with the latter but has an opposite phase. For the harbors with other topographies, the phenomena shown in Fig. 9 can also be clearly observed. Given the limited space of the paper, the evolutions of the maximum free surface elevations inside the harbors with other topographies exposed to the LDN waves are not presented here.

4.2. Maximum runup inside the harbor

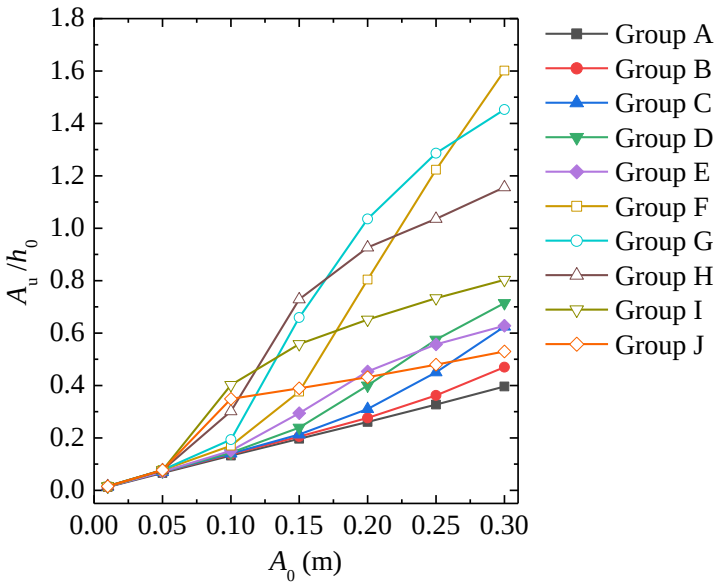

Fig. 10. The normalized maximum runups inside the harbor, A_u/h_0, in all numerical experiments

Fig. 10 presents the normalized maximum runups inside the harbor, A_u/h_0, in all numerical experiments. As expected, for all groups, the maximum runups inside the harbor increase monotonously with the increase of the incident wave amplitude A_0. It is also seen that when the incident wave amplitude is small (i.e., $A_0 \leq 0.05$ m), the maximum runup inside the harbor is almost only determined by the incident wave amplitude, and the influences of both the incident N-wave type and the bottom profile inside the harbor seem to be negligible. However, as the

incident wave amplitude further increases (i.e., 0.05 m < $A_0 \leq$ 0.3 m), the variation curve of the maximum runup becomes closely related to both the incident wave type and the bottom profile inside the harbor. For the effects of the N-wave type, it is clear that for each bottom profile, the maximum runups excited by the LDN wave are in general remarkably larger than those induced by the LEN wave. As for the influences of the bottom profile inside the harbor, they will be elaborated below.

The phenomena shown in Fig. 10 can be qualitatively explained as follows. Based on the investigations of Zhao et al. (2010) and Zhao (2011) on the propagation properties of the N-waves in the sea of various water depths, it was found that when the wave amplitude of the incident N-waves is extremely small compared with the water depth, the wave profiles of the LEN and LDN waves can keep the same as the initial waveforms during the propagation. This reasonably explains why the maximum runup inside the harbor is insensitive to the incident N-wave type when $A_0 \leq$ 0.05 m. As for the insensitivity of the maximum runup to the bottom profile under condition of $A_0 \leq$ 0.05 m, it can probably be attributed to the equilibrium between the shoaling effect and the reflection effect over the uneven topographies. The shoaling effect of the incident N-waves over various bottom profiles tends to intensify the maximum runup inside the harbor; the smaller the mean water depth is, the more obvious the intensification effect is. On the other hand, due to the existence of various bottom profiles, there exists the energy reflection of the incident N-waves as they propagate over the bottom inside the harbor, which can weaken the maximum runup of the incident waves inside the harbor. Based on the results that will be shown in Section 4.3.3, when $A_0 \leq$ 0.05 m, the reflected wave energy gradually increases with the decrease of the mean water depth overall, which means that the smaller mean water depth tends to cause the smaller maximum runup inside the harbor.

Zhao et al. (2010) and Zhao (2011) also found that for the incident N-waves with larger relative amplitude, their wave profiles during the propagation cannot keep the same as the initial waveform anymore because of the dispersive effect, and the larger relative amplitude leads to a faster and greater wave deformation. In addition, for the LEN and LDN waves, their waveform evolutions during the propagation present different characteristics (Zhao, 2011; Zhao et al., 2010). The faster and greater wave deformation and the different waveform evolution characteristics of the LEN and LDN waves lead to the dependence of the maximum runup on both the incident

wave height and the bottom profile inside the harbor when A_0 > 0.05 m. In fact, the different waveform evolution characteristics of the LEN and LDN waves also reasonably account for the different evolution features for the maximum free surface elevations of the incident LEN and LDN waves shown in Figs. 8 and 9.

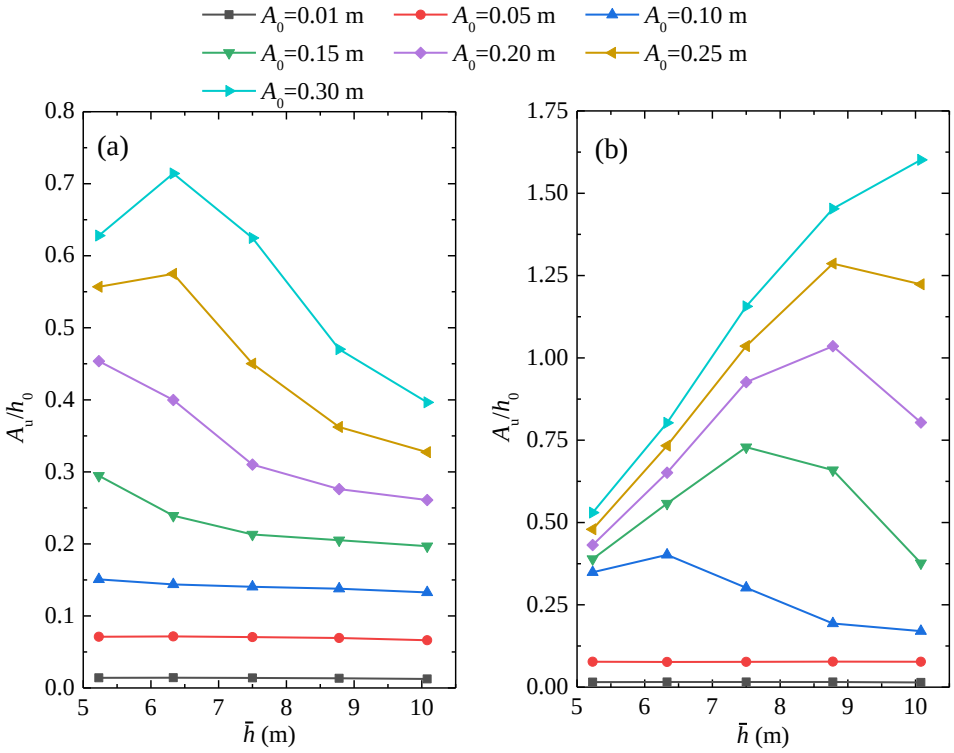

Fig. 11. Variations of the normalized maximum runups, A_u/h_0, with respect to the mean water depth inside the harbor, $\bar{h}$, excited by (a) the incident LEN waves and (b) the incident LDN waves.

To better present the influences of the bottom profile inside the harbor on the maximum runup, Fig. 11 illustrates the variations of the normalized maximum runups, A_u/h_0, with respect to the mean water depth inside the harbor, $\bar{h}$, excited by the incident LEN and LDN waves. Identical to the phenomenon in Fig. 10, when $A_0 \leq 0.05$ m, the bottom profile inside the harbor has almost no significant impact on the maximum runup. However, when the incident wave amplitude becomes larger, the influences of the bottom profile inside the harbor on the maximum runup closely depend on both the incident wave type and the incident wave amplitude. For the incident LEN waves (Fig. 11a), when 0.10 m $\leq A_0 \leq$ 0.20 m, the maximum runups increase gradually with

the decrease of the mean water depth inside the harbor, $\bar{h}$. As the incident wave amplitude further increases (i.e., 0.25 m $\leq A_0 \leq$ 0.30 m), at the range of 6.33 m $\leq \bar{h} \leq$ 10.08 m, the maximum runups inside the harbor are still shown to increase monotonously with the decrease of $\bar{h}$. However, as $\bar{h}$ further decreases, the maximum runups inside the harbor begin to decline. For the incident LDN waves (Fig. 11b), when 0.10 m $\leq A_0 \leq$ 0.25 m, the maximum runups inside the harbor are also shown to increase first and then decrease with the decrease of $\bar{h}$. In addition, as the incident wave amplitude increases, the range of the mean water depth at which the maximum runup decreases with the decrease of $\bar{h}$ becomes larger and larger. As the incident LDN wave increases to the largest wave amplitude (i.e., A_0=0.30 m), the maximum runup inside the harbor completely presents a monotone decrease with the decrease of $\bar{h}$.

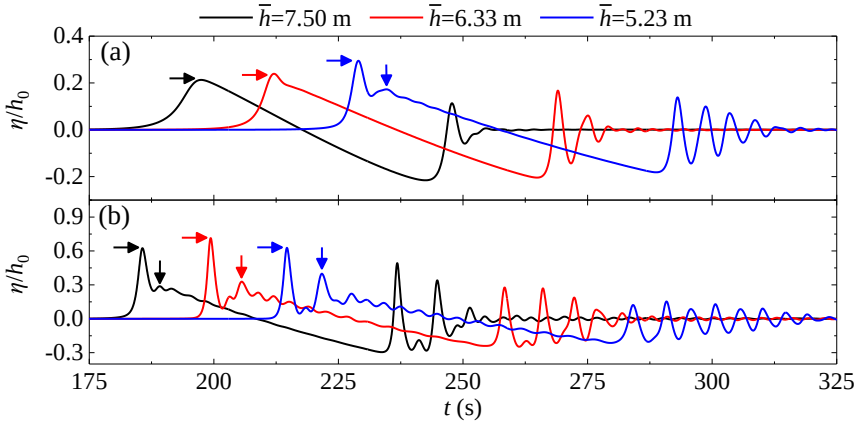

Fig. 12. Time series of the free surface elevations at gauge G_{151} for different bottom profiles inside the harbor excited by the LEN waves with (a) A_0=0.15 m and (b) A_0=0.30 m. The leading crests and the secondary crests of the free surface elevations are marked out by the horizontal and the vertical arrows, respectively.

To further explain why the changing trends of the maximum runup inside the harbor with respect to $\bar{h}$ are different at the ranges of 0.10 m $\leq A_0 \leq$ 0.20 m and 0.25 m $\leq A_0 \leq$ 0.30 m shown in Fig. 11a, the time series of the free surface elevations at gauge G_{151} for different bottom profiles inside the harbor excited by the LEN waves with A_0=0.15 m and 0.30 m are demonstrated in Fig. 12. When A_0=0.15 m (Fig. 12a), it is seen that the shallower mean water depth inside the harbor leads to larger maximum runup over the backwall of the harbor. It coincides with the general rule

of the wave shoaling in the nearshore areas that the wave amplitude/height of the incident waves becomes gradually larger as they propagate from the deeper to the shallower water (Mei, 1983). Although there exists a secondary crest for the smallest mean water depth (i.e., $\bar{h}$ =5.23 m), which can weaken the energy possessed by the leading crest and hence decrease the maximum runup to some extent, the maximum runup for $\bar{h}$ =5.23 m is still larger than those for $\bar{h}$ =6.33 m and 7.50 m. While when A_0=0.30 m (Fig. 12b), all the three time series of the free surface elevations at gauge G_{151} possess both the leading and the secondary crests; the smaller the mean water depth is, the more obvious the secondary crest becomes. The maximum runup inside the harbor is jointly determined by the wave shoaling and the secondary crest. When $\bar{h}$ decreases from 7.50 m to 6.33 m, the incremental effect of the wave shoaling is stronger than the attenuation effect of the secondary crest. Hence, the maximum runup inside the harbor shows an increase with the decrease of $\bar{h}$. However, when $\bar{h}$ decreases further from 6.33 m to 5.23 m, the incremental effect of the wave shoaling becomes weaker than the attenuation effect of the secondary crest. Therefore, the maximum runup inside the harbor shows a decrease with the decrease of $\bar{h}$.

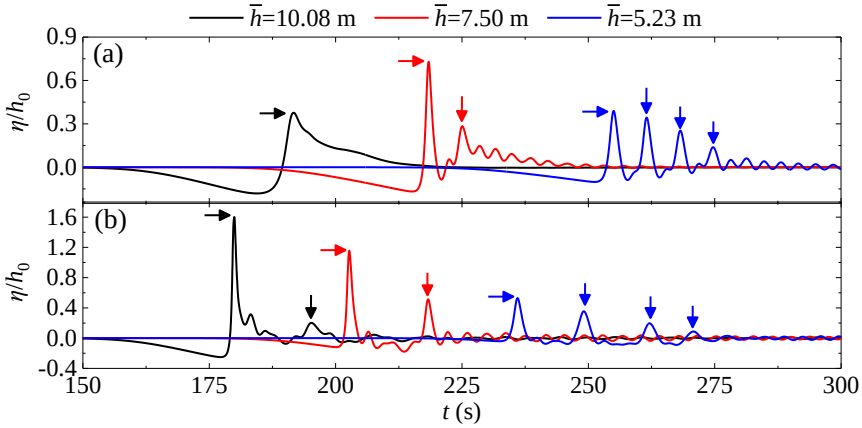

Fig. 13. Time series of the free surface elevations at gauge G_{151} for different bottom profiles inside the harbor excited by the LDN waves with (a) A_0=0.15 m and (b) A_0=0.30 m. The leading crests and the secondary crests of the free surface elevations are marked out by the horizontal and the vertical arrows, respectively.

Similarly, to further explain why the tendency of the maximum runup inside the harbor with respect to $\bar{h}$ are different at the range of 0.10 m ≤ A_0 ≤ 0.25 m and at A_0 =0.30 m shown in Fig.

11b, the time series of the free surface elevations at gauge G_{151} for various topographies inside the harbor excited by the LDN waves with A_0=0.15 m and 0.30 m are presented in Fig. 13. When A_0=0.15 m (Fig. 13a), the maximum runup is also jointly determined by the wave shoaling and the secondary crest. When $\bar{h}$ decreases from 10.08 m to 7.50 m, the incremental effect of the wave shoaling is stronger than the attenuation effect of the secondary crest; the maximum runup shows an increase with the decrease of $\bar{h}$. On the contrary, when $\bar{h}$ decreases further from 7.50 m to 5.23 m, the incremental effect of the wave shoaling becomes weaker than the attenuation effect of the secondary crest; the maximum runup shows a decrease with the decrease of $\bar{h}$. For the smallest mean water depth (i.e., $\bar{h}$ =5.23 m), there exist three secondary crests in the time series of the free surface elevation, rather than just one secondary crest as for $\bar{h}$ =7.50 m. When A_0=0.30 m (Fig. 13b), the attenuation effect of the secondary crest has become a decisive factor for the maximum runup inside the harbor. The smaller mean water depth causes a more obvious secondary crest or a larger number of secondary crests. Hence, the maximum runup inside the harbor gradually decreases with the decrease of $\bar{h}$.

4.3. Relative wave energy distribution and total wave energy inside the harbor

4.3.1. Computational procedure for response amplitudes of different resonant modes

As stated in Section 2.2, to analyze the relative wave energy distribution and the total wave energy inside the harbor during transient harbor oscillations, the NMD method is essential to be adopted. This section elaborates the specific computational procedure for the response amplitudes of different resonant modes by using the data analysis method. The time series of the free surface elevations at gauge G_{01} for the two cases in Groups C and H with A_0=0.05 m are presented in Fig. 14. Only the wave climates within the time period between t_0 and t_1 are utilized to separate the response amplitudes of various modes. t_0 denotes the moment that the incident N-wave entirely propagates into the harbor from the open sea, and t_1 refers to the moment that the reflected N-wave from the backwall starts to spread out of the harbor. It can be observed from this figure that the incident N-waves for both cases entirely propagates into the harbor at t_0=135 s, and the reflected waves from the backwall start to spread out of the harbor at t_1=350 s.

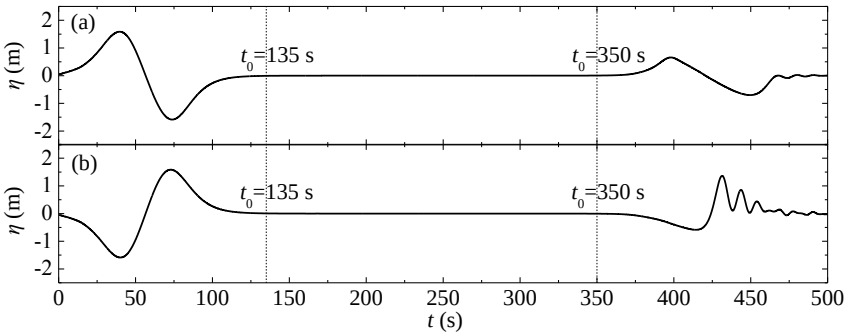

Fig. 14. Time series of the free surface elevations at gauge G_{01} for the two cases in (a) Group C and (b) Group H with A_0=0.05 m.

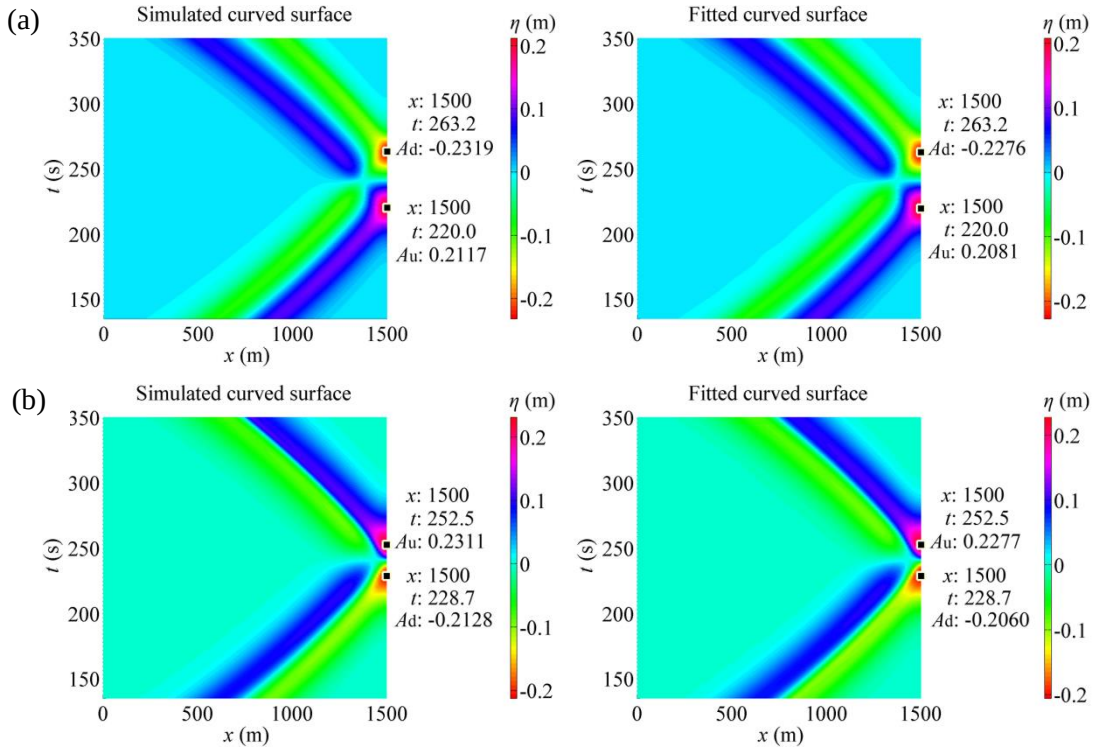

Fig. 15. The simulated and the corresponding fitted free surfaces for the two cases in (a) Group C and (b) Group H with A_0=0.05 m.

Fig. 15 presents the comparison of the simulated and the corresponding fitted free surfaces for the two cases in Fig. 14. The former is directly obtained through the numerical simulations of FUNWAVE-TVD, while the latter is gained by the NMD method. The lowest forty modes are taken into consideration during fitting the simulated free surface. For both cases, there exists a good coincidence between the simulated and the fitted free surfaces. For the case in Group C with A_0=0.05 m (Fig. 15a), the simulated free surface has a maximum rundown of -0.2319 m at x=1500

m and t=263.2 s and has a maximum runup of 0.2117 m at x=1500 m and t=220.0 s; at the identical position and the identical time, the fitted free surface has a maximum rundown of -0.2276 m and a maximum runup of 0.2018 m. For the case in Group H with A_0=0.05 m (Fig. 15b), the simulated free surface has a maximum rundown of -0.2128 m at x=1500 m and t=228.7 s and has a maximum runup of 0.2311 m at x=1500 m and t=252.5 s; at the identical position and the identical time, the fitted free surface a maximum rundown of -0.2060 m and has a maximum runup of 0.2277 m.

Table 3. Numerical fitting errors (*NFE*s) of the NMD method for all the cases with A_0=0.01 m and 0.05 m.

A_0 (m)	Group									
	A	B	C	D	E	F	G	H	I	J
0.01	0.43%	0.10%	0.19%	0.49%	0.01%	0.86%	0.15%	0.31%	0.31%	0.25%
0.05	1.21%	1.53%	1.85%	1.96%	3.85%	2.01%	2.56%	3.19%	3.99%	4.22%

Identical to Gao et al. (2017), considering the typicality and importance of the maximum rundown/runup, the numerical fitting error (*NFE*) of the data analysis method is defined as the maximum percentage error between the maximum values of the simulated and the fitted rundown/runup, namely,

$$NFE = \max\left\{ \left| \left[A_{\mathrm{d}} - (A_{\mathrm{d}})_{\mathrm{fitted}} \right] / A_{\mathrm{d}} \right|, \left| \left[A_{\mathrm{u}} - (A_{\mathrm{u}})_{\mathrm{fitted}} \right] / A_{\mathrm{u}} \right| \right\} \times 100\% , \tag{16}$$

where A_{d} and A_{u} refer to the maximum rundown and maximum runup obtained by the numerical simulations, respectively; $(A_{\mathrm{d}})_{\mathrm{fitted}}$ and $(A_{\mathrm{u}})_{\mathrm{fitted}}$ refer to the maximum rundown and maximum runup fitted by the NMD method, respectively. The *NFE* can directly embody the computational accuracy of the data analysis method in calculating the response amplitudes of different modes. The *NFE*s for these two cases in Groups C and H with A_0=0.05 m are 1.85% and 3.19%, respectively. The *NFE*s for all the cases with A_0=0.01 m and 0.05 m are further listed in Table 3. It is observed that the *NFE*s for all these cases are less than 4.30%, which assures the precise estimation of the response amplitudes of various modes. The calculated response amplitudes of various modes for all these cases will be presented in Section 4.3.2.

4.3.2. Relative wave energy distribution over various resonant modes

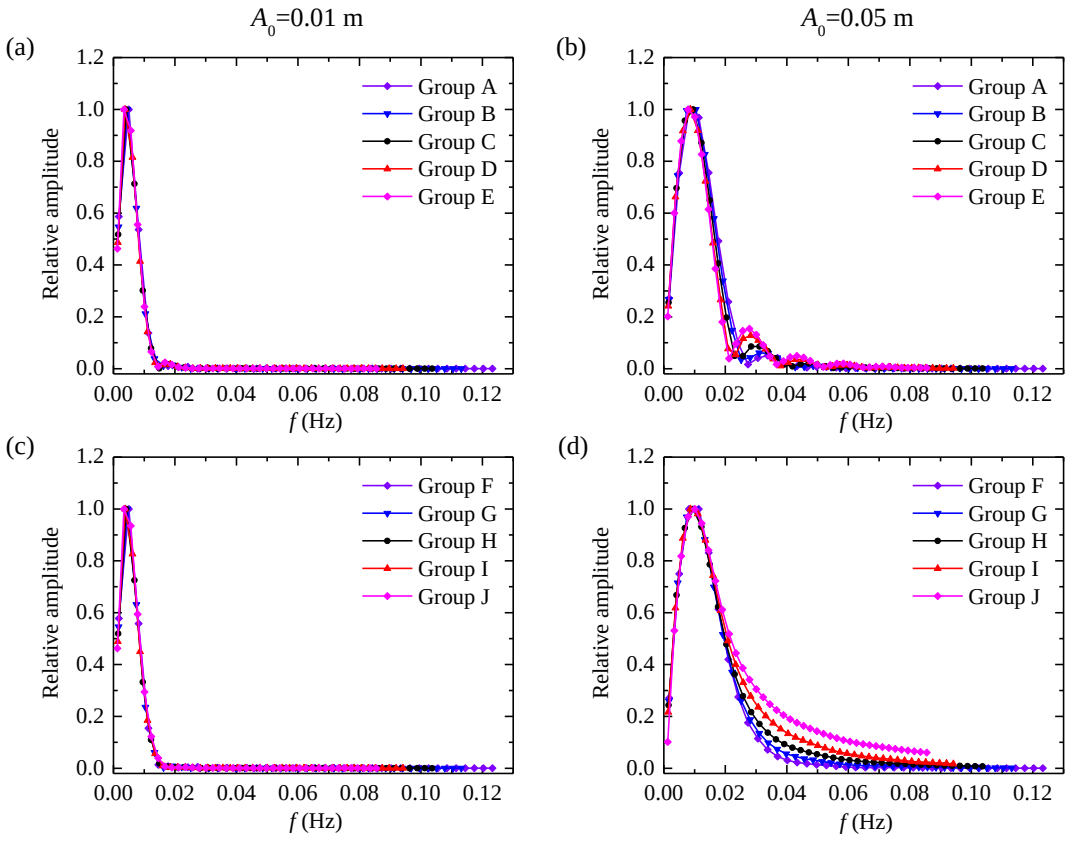

Fig. 16. Relative amplitudes of the lowest forty modes inside harbors with various bottom profiles. (a) and (b) correspond to the incident LEN waves with A_0=0.01 m and 0.05 m, respectively; (c) and (d) correspond to the incident LDN waves with A_0=0.01 m and 0.05 m, respectively.

To better present the relative wave energy distribution over various resonant modes, for all the twenty cases listed in Table 3, the response amplitude of each mode is normalized by the corresponding maximum response amplitude, and the normalized response amplitude is called as "relative amplitude", i.e.,

$$\bar{A}_i = \frac{A_i}{\max(A_i)} \quad (i = 1, 2, ..., 40), \tag{17}$$

where A_i (i=1, 2,…, 40) denotes the response amplitude of the i-th mode. Fig. 16 demonstrates the relative amplitudes of the lowest forty modes for all the cases with A_0=0.01 m and 0.05 m. It is clear that both the incident wave amplitude and the bottom profile inside the harbor have significant effects on the relative wave energy distribution. First, for the effects of the incident wave amplitude, it can be observed that when the incident wave amplitude is small (i.e., A_0=0.01

m) (Fig. 16a and c), the overwhelming majority of the wave energy inside the harbor is concentrated in the lowest five modes, and only a very small fraction of the wave energy is distributed over the higher resonant modes. However, as the incident wave amplitude rises to A_0=0.05 m (Fig. 16b and d), most of the wave energy is distributed among more modes. Hence, the wave energy distribution over various modes is inclined to become more uniform for the larger incident N-wave overall. Second, for the influences of the bottom profile inside the harbor, observing Fig. 16b and d can also find that when the incident wave amplitude equals A_0=0.05 m, the proportion of the wave energy distributed over higher modes gradually increases with the decrease of the mean water depth inside the harbor, $\bar{h}$. In general, the wave energy distribution over various modes also becomes more uniform as $\bar{h}$ decreases.

To better compare the uniformity of the wave energy distribution under different incident wave amplitudes and different bottom profiles and to further compare the wave energy distributions under different incident N-wave types (i.e., LEN and LDN waves), it is essential to further quantify the uniformity of the wave energy distribution inside the harbor. The coefficient of variance (*CV*) of the response amplitudes of the lowest forty resonant modes is adopted in this paper and is calculated as follows:

$$CV = \frac{\sigma}{\mu}, \tag{18}$$

where

$$\sigma = \sqrt{\frac{1}{40}\sum_{i=1}^{40}\left(A_i - \mu\right)^2}, \tag{19}$$

and

$$\mu = \frac{1}{40}\sum_{i=1}^{40} A_i . \tag{20}$$

Obviously, the *CV* value can embody the deviation degree of the response amplitudes of various modes relative to their average value more directly, and the smaller *CV* value means the greater uniformity of the wave energy distribution over various resonant modes.

Fig. 17 presents the *CV* values of the response amplitudes of the lowest forty modes for all the twenty cases shown in Fig. 16. Three obvious phenomena can be easily observed. First, for both the LEN and LDN waves, the *CV* value for the smaller incident wave amplitude is always shown to be significantly higher than that for the larger incident wave amplitude, which is

consistent with the qualitative finding in Fig. 16. Second, the *CV* value always decreases with the decrease of the mean water depth inside the harbor, $\bar{h}$, regardless of the incident wave amplitude and the incident N-wave type. This is also in accord with the corresponding qualitative finding in Fig. 16. Third, for both the incident wave amplitudes considered here, the *CV* values of the LDN waves are consistently less than those of the LEN waves, which indicates that the uniformity of the wave energy distributions excited by the LDN waves is always greater than that excited by the LEN waves under condition of the same bottom profile. In addition, compared with the *CV* values of the LEN waves, the descent degree of the *CV* values of the LDN waves for the larger incident wave amplitude (i.e., A_0=0.05 m) is remarkably higher than that for the smaller incident wave amplitude (i.e., A_0=0.01 m). This indicates that the influencing degree of the incident N-wave type on the wave energy distribution inside the harbor closely depends on the incident wave amplitude, and the larger the incident wave amplitude is, the more obvious the influence of the incident wave type on the wave energy distribution becomes. It should be noted that, similar to the maximum free-surface elevation evolution in Section 4.1 and the maximum runup inside the harbor in Section 4.2, these differences between the wave energy distribution inside the harbor excited by LEN and LDN waves can also be attributed to their different waveform evolution characteristics revealed in Zhao et al. (2010) and Zhao (2011).

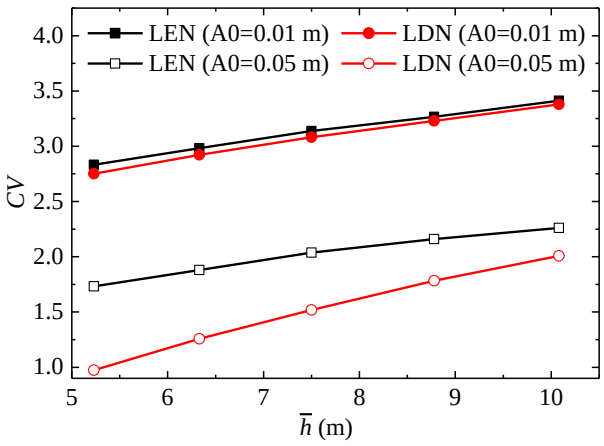

Fig. 17. *CV* values of the response amplitudes of the lowest forty modes for all the twenty cases shown in Fig. 16.

4.3.3. Total wave energy inside the harbor

Due to the fact that the wave climate inside the harbor is a linear superposition of various modes during the transient harbor oscillations induced by tsunamis (Gao et al., 2015; Sobey, 2006), the total wave energy inside the harbor can be estimated by the following expression accurately:

$$E = \sum_{i=1}^{40} \frac{1}{2} A_i^2 . \tag{21}$$

Fig. 18 demonstrates the total wave energy inside the harbor for all the twenty cases shown in Fig. 16. There are two obvious phenomena that can be easily observed from this figure. First, the variation tendency of the total wave energy with respect to the bottom profile depends on the incident wave amplitude. When the incident wave amplitude is small (i.e., A_0=0.01 m) (Fig. 18a), the total wave energy inside the harbor is shown to first increase and then decrease with the increase of the mean water depth inside the harbor, $\bar{h}$, regardless of the incident N-wave type, and it always reaches the maximum value when $\bar{h} = 8.78$ m. Equivalently, from the viewpoint of wave energy reflection inside the harbor, it means that the reflected wave energy first decreases slightly and then gradually increases with the decrease of the mean water depth. However, when the incident wave amplitude increases to A_0=0.05 m (Fig. 18b), the reflected wave energy is shown to gradually decrease with the increase of $\bar{h}$, and the total wave energy inside the harbor is shown to monotonously increase with the increase of $\bar{h}$ correspondingly, no matter whether the incident waves are LEN or LDN waves. Second, it is clear that the variation curves of the total wave energy inside the harbor with the mean water depth for the LEN and LDN waves are very close to each other, especially when the incident wave amplitude is small.

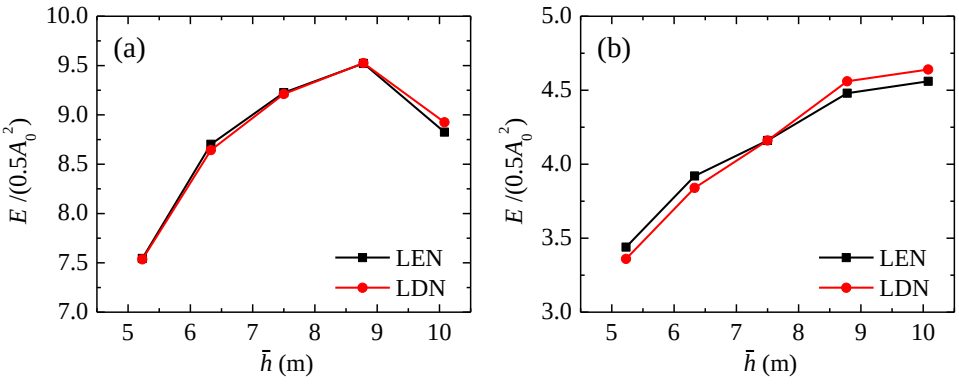

Fig. 18. Normalized total wave energy inside harbors with various topographies for (a) A_0=0.01 m and (b) A_0=0.05 m.

5. Conclusions

In the present work, the transient harbor oscillations triggered by normally-incident LEN and LDN waves with various amplitudes inside elongated rectangular harbors with different bottom profiles are simulated by utilizing the FUNWAVE-TVD model. The effects of the variation of the bottom profile on the wave profile evolution, the maximum runup, the relative wave energy distribution and the total wave energy inside the harbor are first studied comprehensively. The results of this study will enhance the knowledge of the harbor resonance excited by the transient nonlinear long waves, such as tsunamis.

The following conclusions can be drawn from the results of the present study:

1. When the harbor has relatively larger mean water depth and is subjected to the LEN waves, the evolution of the maximum free surface elevation during the wave shoaling process inside the harbor agrees well with Green's law regardless of the incident wave amplitude, except at the area where the incident and the reflected waves interact with each other near the backwall. For the harbor with relatively smaller mean water depth, the applicability of Green's law becomes closely related to the incident wave amplitude; the larger the incident wave amplitude is, the smaller the valid spatial range of Green's law becomes. When the harbor is exposed to the LDN waves, the evolution of the maximum free surface elevation during the wave shoaling process inside the harbor coincides well with Green's law only for the relatively smaller incident wave amplitude, no matter whether the mean water depth inside the harbor is large or small.
2. When the incident wave amplitude is small, the maximum runup inside the harbor is almost only determined by the incident wave amplitude, and the influences of both the incident N-wave type and the bottom profile inside the harbor seem to be negligible. However, as the incident wave amplitude becomes larger, the influences of the bottom profile inside the harbor on the maximum runup closely depend on both the incident wave type and the incident wave amplitude.
3. The relative wave energy distribution inside the harbor tends to become more uniform as the

incident wave amplitude increases. The similar tendency is also observed as the mean water depth inside the harbor gradually decreases, regardless of the incident wave amplitude and the incident N-wave type. In addition, for identical incident wave amplitudes, the relative wave energy distributions excited by the LDN waves are more uniform than those triggered by the LEN waves.

4. The variation tendency of the total wave energy inside the harbor with the bottom profile depends on the incident wave amplitude. When the incident wave amplitude is small (i.e., A_0=0.01 m), the total wave energy inside the harbor first increases and then decreases with the increase of the mean water depth inside the harbor. However, when the incident wave amplitude increases to A_0=0.05 m, the total wave energy becomes to monotonously increase with the increase of the mean water depth. In addition, the variation curves of the total wave energy with the mean water depth for the incident LEN and LDN waves are very close to each other, especially when the incident wave amplitude is small.

Finally, we reaffirm that these conclusions are only valid for the elongated harbors, the types of the incident N-waves and the variation ranges of the incident wave amplitude and the mean water depth inside the harbor considered in this paper.

Acknowledgments

This research is financially supported by the National Key Research and Development Program (2017YFC1404200), the National Natural Science Foundation of China (Grant Nos. 51911530205, 51609108 and 51679113), the Royal Society of UK (Grant No. IEC\NSFC\181321), the Jiangsu Government Scholarship for Overseas Studies (awarded to Dr. Junliang Gao for study abroad at the University of Bath), the Natural Science Foundation of Jiangsu Province of China (Grant No. BK20170576) and the Natural Science Research of Jiangsu Higher Education Institutions of China (Grant No. 17KJB580006).

References

Bellotti, G., Briganti, R., Beltrami, G.M., 2012. The combined role of bay and shelf modes in tsunamis amplification along the coast. Journal of Geophysical Research: Oceans 117, C08027, doi: 10.1029/2012JC008061.

Byatt-Smith, J.G.B., 1971. An integral equation for unsteady surface waves and a comment on the Boussinesq equation. Journal of Fluid Mechanics 49 (4), 625-633.

Camfield, F., Street, R., 1969. Shoaling of solitary waves on small slopes. J. Waterways and Harbours Div. 95, 1-22.

Charvet, I., Eames, I., Rossetto, T., 2013. New tsunami runup relationships based on long wave experiments. Ocean Modelling 69, 79-92.

Chen, Q., 2006. Fully nonlinear Boussinesq-type equations for waves and currents over porous beds. Journal of Engineering Mechanics 132 (2), 220-230.

De Jong, M.P.C., Battjes, J.A., 2004. Seiche characteristics of Rotterdam Harbour. Coastal Engineering 51 (5-6), 373-386.

Dong, G., Wang, G., Ma, X., Ma, Y., 2010a. Harbor resonance induced by subaerial landslide-generated impact waves. Ocean Engineering 37 (10), 927-934.

Dong, G., Wang, G., Ma, X., Ma, Y., 2010b. Numerical study of transient nonlinear harbor resonance. Science China-Technological Sciences 53, 558-565.

Fabrikant, A.L., 1995. Harbor oscillations generated by shear flow. Journal of Fluid Mechanics 282, 203-217.

Gao, J., Ji, C., Gaidai, O., Liu, Y., Ma, X., 2017. Numerical investigation of transient harbor oscillations induced by N-waves. Coastal Engineering 125, 119-131.

Gao, J., Ji, C., Liu, Y., Gaidai, O., Ma, X., Liu, Z., 2016a. Numerical study on transient harbor oscillations induced by solitary waves. Ocean Engineering 126, 467-480.

Gao, J., Ji, C., Liu, Y., Ma, X., Gaidai, O., 2018a. Numerical study on transient harbor oscillations induced by successive solitary waves. Ocean Dynamics 68 (2), 193-209.

Gao, J., Ma, X., Dong, G., Wang, G., Ma, Y., 2015. Improvements on the normal mode decomposition method used in harbor resonance. Proc IMechE Part M: Journal of Engineering for the Maritime Environment 229 (4), 397-410.

Gao, J., Ma, X., Dong, G., Wang, G., Ma, Y., 2016b. Numerical study of transient harbor resonance induced by solitary waves. Proc IMechE Part M: Journal of Engineering for the Maritime Environment 230 (1), 163–176.

Gao, J., Zhou, X., Zang, J., Chen, Q., Zhou, L., 2018b. Influence of offshore fringing reefs on infragravity period oscillations within a harbor. Ocean Engineering 158, 286-298.

Gao, J., Zhou, X., Zhou, L., Zang, J., Chen, H., 2019. Numerical investigation on effects of fringing reefs on low-frequency oscillations within a harbor. Ocean Engineering 172, 86-95.

Goring, D.G., 1978. Tsunamis - the propagation of long waves onto a shelf. Ph.D. dissertation, W. M. Keck Laboratory of Hydraulics and Water Resources, California Institute of Technology, Pasadena, California.

Hsiao, S.-C., Hsu, T.-W., Lin, T.-C., Chang, Y.-H., 2008. On the evolution and run-up of breaking solitary waves on a mild sloping beach. Coastal Engineering 55, 975-988.

Kennedy, A.B., Kirby, J.T., Chen, Q., Dalrymple, R.A., 2001. Boussinesq-type equations with improved nonlinear performance. Wave Motion 33, 225-243.

Kumar, P., Gulshan, 2018. Theoretical analysis of extreme wave oscillation in Paradip Port using a 3-D boundary element method. Ocean Engineering 164, 13-22.

Kumar, P., Zhang, H., Kim, K.I., Yuen, D.A., 2016. Modeling wave and spectral characteristics of moored ship motion in Pohang New Harbor under the resonance conditions. Ocean Engineering 119, 101-113.

López, M., Iglesias, G., 2014. Long wave effects on a vessel at berth. Applied Ocean Research 47, 63-72.

Liu, P.L.-F., Cho, Y.-S., Briggs, M.J., Kanoglu, U., Synolakis, C.E., 1995. Runup of solitary waves on a circular island. Journal of Fluid Mechanics 302, 259-285.

Liu, P.L.-F., Monserrat, S., Marcos, M., Rabinovich, A.B., 2003. Coupling between two inlets: Observation and modeling. Journal of Geophysical Research: Oceans 108, C3, 3069, doi:10.1029/2002JC001478.

Lo, H.-Y., Park, Y.S., Liu, P.L.-F., 2013. On the run-up and back-wash processes of single and double solitary waves - An experimental study. Coastal Engineering 80, 1-14.

Ma, G., Shi, F., Kirby, J.T., 2012. Shock-capturing non-hydrostatic model for fully dispersive surface wave processes. Ocean Modelling 43-44, 22–35.

Madsen, P.A., Fuhrman, D.R., Schäffer, H.A., 2008. On the solitary wave paradigm for tsunamis. Journal of Geophysical Research: Oceans 113, C12012, doi:10.1029/2008JC004932.

Madsen, P.A., Schäffer, H.A., 2010. Analytical solutions for tsunami runup on a plane beach single waves, N-waves and transient waves. Journal of Fluid Mechanics 645, 27-57.

Mei, C.C., 1983. The Applied Dynamics of Ocean Surface Waves. Wiley, New York.

Okihiro, M., Guza, R.T., 1996. Observations of seiche forcing and amplification in three small harbors. Journal of Waterway, Port, Coastal and Ocean Engineering 122 (5), 232-238.

Pattiaratchi, C.B., Wijeratne, E.M.S., 2009. Tide gauge observations of 2004-2007 Indian Ocean tsunamis from Sri Lanka and Western Australia. Pure and Applied Geophysics 166 (1), 233-258.

Rabinovich, A.B., 2009. Seiches and harbor oscillations, in: Kim, Y. (Ed.), Handbook of Coastal and Ocean Engineering. World Scientific Publishing, Singapore, pp. 193-236.

Seiffert, B., Hayatdavoodi, M., Ertekin, R.C., 2014. Experiments and computations of solitary-wave forces on a coastal-bridge deck. Part I: Flat Plate. Coastal Engineering 88, 194-209.

Shi, F., Kirby, J.T., Harris, J.C., Geiman, J.D., Grilli, S.T., 2012. A high-order adaptive time-stepping TVD solver for Boussinesq modeling of breaking waves and coastal inundation. Ocean Modelling 43-44, 36-51.

Sobey, R.J., 2006. Normal mode decomposition for identification of storm tide and tsunami hazard. Coastal Engineering 53, 289-301.

Su, S.-F., Ma, G., Hsu, T.-W., 2015. Boussinesq modeling of spatial variability of infragravity waves on fringing reefs. Ocean Engineering 101, 78-92.

Synolakis, C.E., 1987. The runup of solitary waves. Journal of Fluid Mechanics 185, 523-545.

Tadepalli, S., Synolakis, C.E., 1994. The run-up of N-waves on sloping beaches. Proceedings of the Royal Society London A: Mathematical, Physical & Engineering Sciences 445, 99-112.

Wang, G., Dong, G., Perlin, M., Ma, X., Ma, Y., 2011. Numerical investigation of oscillations within a harbor of constant slope induced by seafloor movements. Ocean Engineering 38 (17-18), 2151-2161.

Wang, G., Zheng, J.-H., Maa, J.P.-Y., Zhang, J.-S., Tao, A.-F., 2013. Numerical experiments on transverse oscillations induced by normal-incident waves in a rectangular harbor of constant slope. Ocean Engineering 57, 1-10.

Wang, G., Zheng, J., Liang, Q., Zheng, Y., 2014. Analytical solutions for oscillations in a harbor with a hyperbolic-cosine squared bottom. Ocean Engineering 83, 16-23.

Yao, Y., He, F., Tang, Z., Liu, Z., 2018a. A study of tsunami-like solitary wave transformation and run-up over fringing reefs. Ocean Engineering 149, 142-155.

Yao, Y., Tang, Z., Jiang, C., He, W., Liu, Z., 2018b. Boussinesq modeling of solitary wave run-up reduction by emergent vegetation on a sloping beach. Journal of Hydro-environment Research 19,

78-87.

Zhao, X., 2011. Numerical Simulation of Generation, Propagation and Runup of Tsunamis. Ph.D Dissertation, Shanghai Jiao Tong University, Shanghai.

Zhao, X., Wang, B., Liu, H., 2010. Propagation and runup of tsunami waves with Boussinesq model, Proceedings of the 32nd International Conference on Coastal Engineering (ICCE) Shanghai, China.

Zhao, X., Wang, B., Liu, H., 2012. Characteristics of tsunami motion and energy budget during runup and rundown processes over a plane beach. Physics of Fluids 24 (6), 062107.